

UC Santa Cruz

UC Santa Cruz Previously Published Works

Title

A feedback control architecture for bioelectronic devices with applications to wound healing

Permalink

<https://escholarship.org/uc/item/5z41v8f9>

Journal

Journal of The Royal Society Interface, 18(185)

ISSN

1742-5689

Authors

Jafari, Bashir Hosseini

Zlobina, Ksenia

Marquez, Giovanni

et al.

Publication Date

2021-12-01

DOI

10.1098/rsif.2021.0497

Copyright Information

This work is made available under the terms of a Creative Commons Attribution License, available at <https://creativecommons.org/licenses/by/4.0/>

Peer reviewed

Research



Cite this article: Hosseini Jafari B, Zlobina K, Marquez G, Jafari M, Selberg J, Jia M, Rolandi M, Gomez M. 2021 A feedback control architecture for bioelectronic devices with applications to wound healing. *J. R. Soc. Interface* **18**: 20210497.
<https://doi.org/10.1098/rsif.2021.0497>

Received: 15 June 2021

Accepted: 3 November 2021

Subject Category:

Life Sciences—Engineering interface

Subject Areas:

bioengineering, biotechnology, systems biology

Keywords:

feedback control, wound healing, bioelectronic devices

Author for correspondence:

Marcella Gomez

e-mail: mgomez26@ucsc.edu

A feedback control architecture for bioelectronic devices with applications to wound healing

Bashir Hosseini Jafari¹, Ksenia Zlobina¹, Giovanni Marquez¹,
 Mohammad Jafari², John Selberg³, Manping Jia³, Marco Rolandi³ and
 Marcella Gomez¹

¹Applied Mathematics, Baskin School of Engineering, University of California, Santa Cruz, CA 95064, USA

²Department of Earth and Space Sciences, Columbus State University, Columbus, GA 31907, USA

³Electrical and Computer Engineering, Baskin School of Engineering, University of California, Santa Cruz, CA 95064, USA

MR, 0000-0001-7898-2479; MG, 0000-0001-9709-5015

Bioelectronic devices can provide an interface for feedback control of biological processes in real-time based on sensor information tracking biological response. The main control challenges are guaranteeing system convergence in the presence of saturating inputs into the bioelectronic device and complexities from indirect control of biological systems. In this paper, we first derive a saturated-based robust sliding mode control design for a partially unknown nonlinear system with disturbance. Next, we develop a data informed model of a bioelectronic device for *in silico* simulations. Our controller is then applied to the model to demonstrate controlled pH of a target area. A modular control architecture is chosen to interface the bioelectronic device and controller with a bistable phenomenological model of wound healing to demonstrate closed-loop biological treatment. External pH is regulated by the bioelectronic device to accelerate wound healing, while avoiding chronic inflammation. Our novel control algorithm for bioelectronic devices is robust and requires minimum information about the device for broad applicability. The control architecture makes it adaptable to any biological system and can be used to enhance automation in bioengineering to improve treatments and patient outcomes.

1. Introduction

Bioelectronic devices are a promising technology for precision medicine [1–5]. In particular, bioelectronic devices have been at the centre of smart bandages [6,7]. Many of these bandages have advanced features on board such as sensors to assess the state of wounds in real-time [8,9] and controlled release of therapeutics in a variety of pathological conditions [10–12].

Applying feedback control to enhance the capabilities of smart bandages can help to advance methods in precision medicine [4]. Feedback control is essential to the regulation of natural biological processes and has been considered as an approach to artificially guide or enhance existing biological systems (e.g. artificial pancreas [13,14] and neuro-stimulation [15]). Bioelectronic devices provide an interface between signal processing and biological tissue that allow one to program custom feedback control strategies with sufficient resolution for enhanced performance. To control biological systems, differential voltages are applied to the bioelectronic device in order to drive the delivery or removal of biochemical or biophysical signals to the extracellular environment [11,16,17]. These signalling molecules, in turn, drive cellular response.

A feedback control algorithm then regulates applied voltages based on observed biological response in real-time. In this application, control challenges can arise from indirect control of biological systems, and the presence of

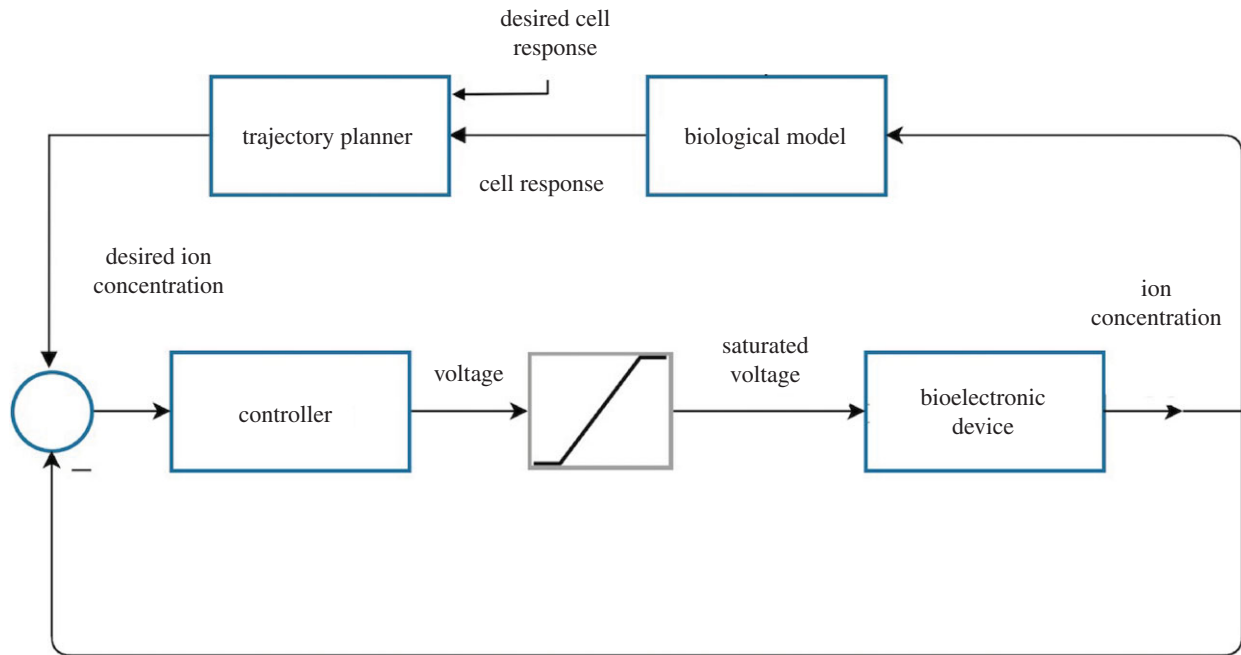


Figure 1. Closed-loop control architecture for a biological model interfaced with a bioelectronic device.

saturation inputs into the bioelectronic device. That is, the bioelectronic device operates reliably only within a bounded range of applied voltages. Voltages outside this range can induce undesired chemical reactions. Researchers have already demonstrated precise spatio-temporal control over delivery of ions using bioelectronic devices [18] and indirect control of stem cell membrane potential through this interface [19]. However, directly addressing saturating inputs into the bioelectronic device in controller design can guarantee convergence for a broader set of conditions and expand capabilities.

Many successful control techniques have already been developed to deal with nonlinear multiple-input multiple-output (MIMO) systems with input saturation. Most of these methods are based on adaptive control [20–22], backstepping [20–22], neural networks (NNs) [23–25] or combinations thereof [24,25]. Although, all the mentioned works above have powerful techniques to address saturation and unknown dynamics, they require optimization, parameter estimation and/or state observers, making them computationally expensive or model-dependent. For example, backstepping approaches require the system to be in a specific form, and the need for the derivative of virtual inputs may cause high complexity. On the other hand, adaptive NNs rely on optimization and assume they can approximate a continuous nonlinear function only in a specific compact set to guarantee convergence, and this assumption might be violated in the first initial steps of optimization in the NNs.

Here, we present a novel control method that takes into consideration saturating signals (bounded input to the bioelectronic device) with minimal information about the device and reduced computational cost for real-time implementation. The method needs no knowledge about system parameter values and only calls for partial information about the system's general input-to-output structure, which can be derived from experiments. To interface the bioelectronic device with a biological system we choose a modular feedback control architecture, where each

component (either the bioelectronic device or the biological system) can be controlled separately and the whole closed-loop system output follows a desired behaviour (figure 1). This architecture lets us replace the biological model in the loop, while keeping the bioelectronic device control design intact for broad applicability.

We apply this method to a bistable phenomenological model of wound healing. We choose wound healing to be our target system because its complexity necessitates a dynamic treatment to account for different needs at each stage of wound healing [26–28]. For example, the wound healing process can be accelerated or prolonged by artificially manipulating pH [29,30] depending on the timing. Here, we consider an *in silico* system where external pH is regulated by the bioelectronic device to accelerate wound healing, while avoiding chronic inflammation. To this end, we model a bioelectronic device known as a proton pump [18,19], where the model parameters are estimated from experimental tests carried out with the proton pump [18]. Finally, we show accelerated wound closure while avoiding chronic condition. We incorporate noise into the simulations to show this approach to be robust to unknown disturbances such as coupling between a bioelectronic device and its biological target.

This paper proceeds as follows. Section 2 formulates a general class of nonlinear systems and our goal is to make the system output follow a desired trajectory. Section 3 presents a novel saturated-based sliding mode control method for the system described in §2, such that the system output converges to the desired value as $t \rightarrow \infty$. In §4, we first model a bioelectronic device and fit parameters to our developed model based on the experimental data. The control algorithm developed in §3 is then applied to the model to regulate ion concentration in a target solution. In §5, we present a bistable wound healing model and discuss how to interconnect that model to an ion pump and controller to avoid chronic situation and accelerate healing. Lyapunov analysis and phase plane trajectory design is used to generate a reference signal for the bioelectronic device. A number of

simulations are conducted in §6 to verify the efficacy of our proposed approach. Finally, we conclude our work in §7.

2. Problem formulation for affine nonlinear systems with input saturation

Bioelectronic devices, as will be verified later in this work, can be approximated by a class of affine nonlinear systems. We first derive a controller for the general case and then apply it to the bioelectronic device.

Consider a MIMO affine nonlinear system with input saturation, represented by the state space model

$$\text{and } \left. \begin{aligned} \dot{x} &= f(x) + G(x)\text{sat}(\varphi(u)) + d(t) \\ y &= h(x), \end{aligned} \right\} \quad (2.1)$$

where $x \in \mathbb{R}^n$ is the state vector of the system, $\text{sat}(\varphi(u)) \in \mathbb{R}^m$ is the control input (to the bioelectronic device in this application), and $y \in \mathbb{R}^p$ ($p \leq n$) is the system output. The function $\varphi(u)$ is applied artificially and designed by the user. As one will note, the incorporation of $\varphi(u)$ facilitates controller design and analysis. Let $f(x) \in \mathbb{R}^n$ be an unknown locally Lipschitz nonlinear function and $G(x) \in \mathbb{R}^{n \times m}$ be an unknown input coefficient matrix. However, we assume the sign value of matrix $G(x)$ is known. Finally, $d(t) \in \mathbb{R}^n$ represents a sufficiently smooth disturbance. The operator $\text{sat}(\cdot) \in \mathbb{R}^m$ is an operator such that

$$\text{sat}(\varphi(u)) = \begin{cases} \varphi(u) & \text{for } s_{\min} < \varphi(u) < s_{\max} \\ s_{\min} & \text{for } \varphi(u) < s_{\min} \\ s_{\max} & \text{for } \varphi(u) > s_{\max}. \end{cases} \quad (2.2)$$

Let the actuating function $\varphi(u)$ take the following form:

$$\varphi(u) = [\varphi_1(u_1) \quad \varphi_2(u_2) \quad \cdots \quad \varphi_m(u_m)]^T \quad (2.3)$$

and be designed by the user such that

$$\varphi_i(\cdot) : \mathbb{R} \rightarrow [s_{\min} \quad s_{\max}]. \quad (2.4)$$

This simplifies $\text{sat}(\varphi(u))$ to $\varphi(u)$. We further expand the general affine class in (2.1) by introducing a new fictitious input $v \in \mathbb{R}^m$ as follows:

$$\text{and } \left. \begin{aligned} \dot{x} &= f(x) + G(x)\varphi(u) + d(t) \\ \dot{u} &= v \\ y &= h(x). \end{aligned} \right\} \quad (2.5)$$

to both mitigate chattering from the sliding mode control design and facilitate finding criteria for tracking convergence. Our goal is to design a bounded function $\varphi_i(\cdot)$, v , and, thus, u such that $y \rightarrow y_d$ when $t \rightarrow \infty$, where $y_d \in \mathbb{R}^p$ is the desired output vector.

3. Feedback control design

In this section, we derive a sliding mode control design for the input saturated system (2.5), and conditions for convergence. Sliding mode is a control technique that constrains the dynamics of a closed-loop system by pushing the system's state trajectories into a manifold. We call this manifold 's' in the paper. The manifold should be designed such that the temporal evolution of the state should converge to the desired state when constrained to the manifold.

3.1. Preliminary derivations

Lemma 3.1. Given the dynamic system (2.5), the second derivative of the state vector x with respect to time can be expressed as

$$\begin{aligned} \ddot{x} &= \nabla_x f(x)\dot{x} + \frac{d}{dt}(G(x)\varphi(u)) + \dot{d}(t) \\ &= \nabla_x f(x)\dot{x} + \frac{d}{dt}(G(x))\varphi(u) + G(x)\frac{d}{dt}(\varphi(u)) + \dot{d}(t) \\ &= \nabla_x f(x)\dot{x} + \frac{d}{dt}(G(x))\varphi(u) + G(x)\nabla_u \varphi(u)\dot{u} + \dot{d}(t) \\ &= \nabla_x f(x)\dot{x} + \psi(x, u)\dot{x} + G(x)\nabla_u \varphi(u)\dot{u} + \dot{d}(t), \end{aligned} \quad (3.1)$$

where the elements of matrix $\psi(x, u) \in \mathbb{R}^{n \times n}$ are functions of φ and partial derivatives of $G(x)$. In particular, the elements of $\psi(x, u)$ are computed as follows:

$$[\psi(x, u)]_{i,j} = \frac{\partial g_i}{\partial x_j} \varphi(u), \quad (3.2)$$

where the vector $g_i(x) = [g_{i1}(x), g_{i2}(x), \dots, g_{im}(x)]$ denotes the i 'th row of the matrix $G(x)$.

Lemma 3.2. Consider the Lyapunov candidate function

$$V = \frac{1}{2} s^T s, \quad (3.3)$$

where

$$\begin{aligned} s &= Kx + \dot{x}, \\ K &= \begin{bmatrix} k_1 & 0 & \cdots & 0 \\ 0 & k_2 & 0 & \cdots & 0 \\ \vdots & 0 & \ddots & \ddots & \vdots \\ & & & k_{n-1} & 0 \\ 0 & \cdots & & 0 & k_n \end{bmatrix}, \end{aligned} \quad (3.4)$$

and $k_i > 0 \forall i$. Note that if $V \rightarrow 0$, then the state dynamics are constrained to $\dot{x} = -Kx$, which converges to zero exponentially by design.

Then we have

$$\dot{V} = s^T \dot{s}, \quad (3.5)$$

where $\dot{s} = K\dot{x} + \ddot{x}$. We substitute the expression for \ddot{x} from lemma 3.1 and get

$$\begin{aligned} \dot{V} &= s^T \dot{s} \\ &= s^T (K\dot{x} + \ddot{x}) \\ &= s^T (K\dot{x} + \nabla_x f(x)\dot{x} + \psi(\cdot)\dot{x} + G(x)\nabla_u \varphi(u)\dot{u} + \dot{d}(t)) \\ &= s^T ((K + \nabla_x f(x) + \psi(\cdot))\dot{x} + G(x)\nabla_u \varphi(u)v + \dot{d}(t)). \end{aligned} \quad (3.6)$$

Let

$$Q^T = G(x)\nabla_u \varphi(u), \quad (3.7)$$

and

$$D = K + \nabla_x f(x) + \psi(x, u), \quad (3.8)$$

then

$$\dot{V} = s^T (D\dot{x} + Q^T v + \dot{d}(t)). \quad (3.9)$$

We now define control laws v and conditions for which $\dot{V} < 0$. We first consider the case of full state feedback under two scenarios. In the first scenario, we assume only partial knowledge of $G(x)$. In particular, we assume we know the signs of elements of $G(x)$. In the second scenario,

we assume full knowledge of $G(x)$ in order to highlight the trade-offs in robustness of the controller. Finally, we consider the case of partial state feedback control under the same two scenarios.

3.2. Full state feedback control

In this section, we consider the case where we want to control the system's states. That is, we have a desired reference for our complete state vector x .

Theorem 3.3. *Let system (2.5) be input-to-state stable (ISS) with origin $O \in \mathbb{R}^n$ in the reachable set and $y = x$. Then, if there exists a scalar $\rho(t) > 0$ such that*

$$\rho(t) > \frac{\|\dot{x}\| \lambda_{\max}(D) + \|\dot{d}\|}{\sqrt{\lambda_{\min}(Q^T Q)}}, \quad (3.10)$$

where $\lambda_{\max}(D)$ and $\lambda_{\min}(Q^T Q)$ are maximum and minimum eigenvalues of matrices D and $Q^T Q$, respectively, the control signal

$$v = -\rho \operatorname{sgn}(Qs), \quad (3.11)$$

guarantees $x \rightarrow 0$ as $t \rightarrow \infty$.

Proof. Substituting the control signal (3.10) into (3.8) gives

$$\dot{V} = s^T (D\dot{x} - \rho Q^T \operatorname{sgn}(Qs) + \dot{d}(t)). \quad (3.12)$$

Using properties of matrix norms it follows that

$$\dot{V} < \|s\| (\|\dot{x}\| \lambda_{\max}(D) - \sqrt{\lambda_{\min}(Q^T Q)} \rho + \|\dot{d}\|). \quad (3.13)$$

Assuming an L_2 norm, we replace $\|s\|$ by $\sqrt{2V}$ from (3.3) to get

$$\dot{V} < \sqrt{2V} (\|\dot{x}\| \lambda_{\max}(D) - \sqrt{\lambda_{\min}(Q^T Q)} \rho + \|\dot{d}\|). \quad (3.14)$$

If ρ satisfies the inequality in (3.9), then the coefficient of \sqrt{V} on the right side of the inequality (3.13) is negative definite. By the comparison lemma and finite time convergence conditions [31], $V \rightarrow 0$ in finite time. Therefore, the system dynamics converge to the designed manifolds formulated in (3.4) in finite time. Furthermore, on that manifold, $x \rightarrow 0$ as $t \rightarrow \infty$. ■

Theorem 3.4. *Let system (2.5) be input-to-state stable (ISS) with origin $O \in \mathbb{R}^n$ in the reachable set and $y = x$. If there exist scalars $\beta > 0$ and $\rho(t) > 0$ such that*

$$\rho(t) > \frac{\|\dot{x}\| \lambda_{\max}(D) - \|s\| \beta \lambda_{\min}(Q^T Q) + \|\dot{d}\|}{\sqrt{\lambda_{\min}(Q^T Q)}}, \quad (3.15)$$

then the control signal

$$v = -\beta Qs - \rho \operatorname{sgn}(Qs) \quad (3.16)$$

guarantees $x \rightarrow 0$ as $t \rightarrow \infty$.

Proof. Substituting control signal (3.15) in (3.8) gives

$$\begin{aligned} \dot{V} &= -\beta s^T Q^T Qs + s^T (D\dot{x} - Q^T \operatorname{sgn}(Qs) \rho + \dot{d}(t)) \\ &< -\beta \lambda_{\min}(Q^T Q) \|s\|^2 + \|s\| (\|\dot{x}\| \lambda_{\max}(D) - \sqrt{\lambda_{\min}(Q^T Q)} \rho + \|\dot{d}\|) \\ &< -\|s\| (\beta \lambda_{\min}(Q^T Q) \|s\| - \|\dot{x}\| \lambda_{\max}(D) + \sqrt{\lambda_{\min}(Q^T Q)} \rho - \|\dot{d}\|). \end{aligned} \quad (3.17)$$

We replace $\|s\|$ with $\sqrt{2V}$ from (3.3) to get

$$\begin{aligned} \dot{V} &< -\sqrt{2V} (\beta \lambda_{\min}(Q^T Q) \|s\| - \|\dot{x}\| \lambda_{\max}(D) \\ &\quad + \sqrt{\lambda_{\min}(Q^T Q)} \rho - \|\dot{d}\|). \end{aligned} \quad (3.18)$$

If ρ satisfies the inequality in (3.14), then the coefficient of \sqrt{V} on the right side of the inequality (3.17) is negative definite. By the comparison lemma and finite time convergence conditions [31], $V \rightarrow 0$ in finite time. Therefore, the system dynamics converge to the designed manifolds formulated in (3.4) in finite time. Furthermore, on that manifold, $x \rightarrow 0$ as $t \rightarrow \infty$. ■

3.3. Output feedback control

In this section, we consider the case where we want to control the system output. The system output can either be simply one of the system's state/s, or a linear/nonlinear combination of system states. In this approach, we define the manifold as

$$s' = Ky + \dot{y}, \quad (3.19)$$

where $K \in \mathbb{R}^{p \times p}$ is a positive definite matrix and $y = h(x) = Cx$, where $C \in \mathbb{R}^{p \times n}$. For example, in our application to the proton pump model, we only consider the concentration of H as the output (to be controlled), and, therefore, can choose C such that y represents the proton concentration. We note that this simplification in the output function holds for a broad set of applications and facilitates proof of output convergence to zero in theorems 3.6 and 3.7.

Lemma 3.5. *Consider the Lyapunov function $V = \frac{1}{2} s'^T s'$. Then*

$$\begin{aligned} \dot{V} &= s'^T \dot{s}' \\ &= s'^T (K\dot{y} + \ddot{y}) \\ &= s'^T (KC\dot{x} + C\ddot{x}) \\ &= s'^T (KC\dot{x} + C(\nabla_x f(x)\dot{x} + \psi(\cdot)\dot{x} + G(x)\nabla_u \varphi(u)\dot{u} + \dot{d}(t))) \\ &= s'^T ((KC + C\nabla_x f(x) + C\psi(\cdot))\dot{x} + CG(x)\nabla_u \varphi(u)\dot{u} + C\dot{d}(t)). \end{aligned} \quad (3.20)$$

Let

$$Q^T = CG(x)\nabla_u \varphi(u), \quad D' = KC + C\nabla_x f(x) + C\psi(\cdot) \quad (3.21)$$

and

$$\dot{d}'(t) = C\dot{d}(t). \quad (3.22)$$

Then

$$\dot{V} = s'^T (D'\dot{x} + Q^T v + \dot{d}'(t)). \quad (3.23)$$

Theorem 3.6. *Let system (2.5) be input-to-state stable (ISS) with origin $O \in \mathbb{R}^n$ in the reachable set and $h(x) = Cx$, where $C \in \mathbb{R}^{p \times n}$. If there exists a scalar $\rho'(t) > 0$ such that*

$$\rho'(t) > \frac{\|\dot{x}\| \lambda_{\max}(D') + \|\dot{d}'\|}{\sqrt{\lambda_{\min}(Q^T Q)}}, \quad (3.24)$$

then, the control signal

$$v = -\rho' \operatorname{sgn}(Q's'), \quad (3.25)$$

guarantees $y \rightarrow 0$ as $t \rightarrow \infty$.

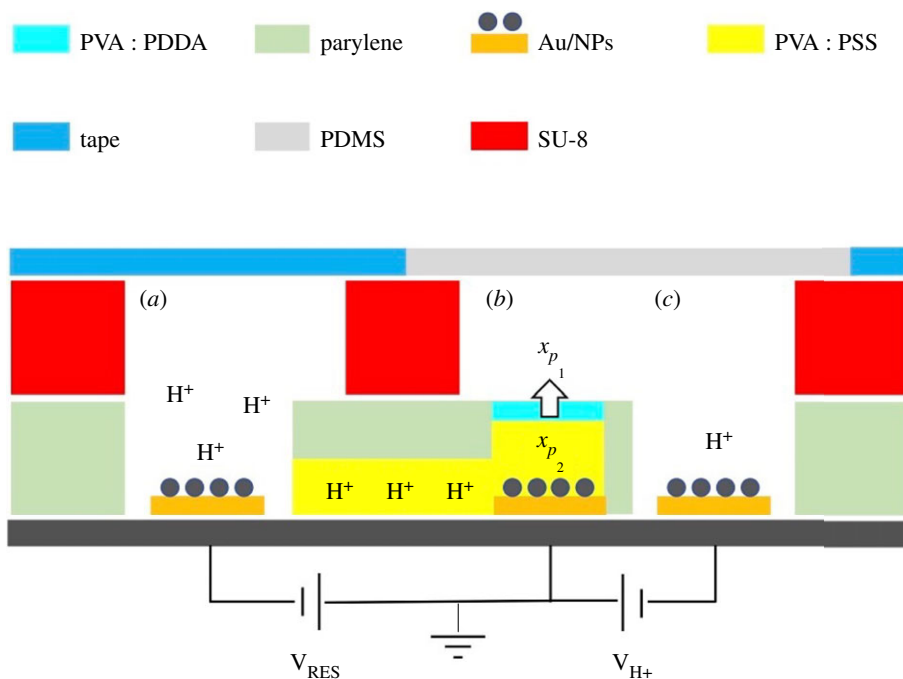


Figure 2. Schematic of a proton pump. Ions can be delivered by applying appropriate differential voltages. Panel (a) represents the reservoir containing ions. Panel (b) represents an area where a voltage can be applied to help regulate the rate of redistribution of ions. Panel (c) represents the target area where microscopic readings are taken. Voltages are applied to individual electrodes here. Au/NPs, gold/nanoparticles; PDDA, poly (diallyldimethylammonium chloride); PDMS, polydimethylsiloxane; PSS, polystyrene sulfonate; PVA, poly vinyl alcohol; SU-8, an epoxy-based negative photoresist.

Proof. The proof follows the same procedure as in theorem 3.3. ■

Theorem 3.7. Let system (2.5) be input-to-state stable (ISS) with origin $O \in \mathbb{R}^n$ in the reachable set and $h(x) = Cx$, where $C \in \mathbb{R}^{p \times n}$. If there exist scalars $\beta' > 0$ and $\rho'(t) > 0$ such that

$$\rho'(t) > \frac{\|\dot{x}\| \lambda_{\max}(D') - \|s'\| \beta' \lambda_{\min}(Q'^T Q') + \|\dot{d}'\|}{\sqrt{\lambda_{\min}(Q'^T Q')}} \quad (3.26)$$

then the control signal

$$v = -\beta' Q' s' - \rho' \text{sgn}(Q' s') \quad (3.27)$$

guarantees $y \rightarrow 0$ as $t \rightarrow \infty$.

Proof. The proof would follow the same procedure as for theorem 3.4. ■

Remark 3.8. In order to meet inequality conditions ((3.9), (3.14), (3.22), (3.24)), matrices $Q^T Q$ and $Q'^T Q'$ should be non-singular.

Remark 3.9. By changing equation (3.4) to

$$s = K(x - x_d) + (\dot{x} - \dot{x}_d), \quad K > 0, \quad (3.28)$$

or, similarly, changing equation (3.18) to

$$s' = K(y - y_d) + (\dot{y} - \dot{y}_d), \quad K > 0, \quad (3.29)$$

we can make $x \rightarrow x_d$, $y \rightarrow y_d$, respectively, as $t \rightarrow \infty$, as long as x_d and y_d are in the reachable set and our system is not time-varying. This result follows from a coordinate transformation [31].

Conditions for convergence in theorems 3.3 and 3.6 might require high gains, which can result in noise amplification or an oscillatory response. At the cost of knowing Q and Q' , we can choose theorems 3.4 and 3.7 for control design with appropriate choices for β and β' to satisfy conditions (3.14) and (3.24), respectively. Note that increasing parameters β and β' , admit lower boundary conditions for ρ and ρ' ,

respectively. The lower boundary conditions cannot be arbitrarily decreased in theorems 3.3 and 3.6.

Actuating function $\varphi(u)$, as long as it is bounded within the saturation thresholds, can be purposefully designed to help us satisfy inequalities ((3.9), (3.14), (3.22), (3.24)). Increasing $\nabla_u \varphi(u)$, increases $\lambda_{\min}(Q^T Q)$, which decreases the lower bound on ρ . A potential trade-off could be increased sensitivity to changes in u , potentially leading to a bang-bang like control scheme.

Finally, we note that \dot{x} and \dot{y} is needed to compute the control signal. It is possible to estimate \dot{x} and \dot{y} with a variety of methods. While these techniques are susceptible to sensor noise, in our case we mitigate the noise effect by filtering the signal after sensing. Our simulations use backwards difference and show satisfactory results.

4. Modelling and control of a bioelectronic device

The feedback control laws developed in the previous sections may be applied to many types of bioelectronic devices. In this section, we apply the control to a family of bioelectronic devices known as ion pumps. In particular, we consider the proton pump described in [18,19]. We develop a dynamical model of the system where parameters are determined using input-to-output response of the device. We first briefly describe the device and the experimental setup used to generate the data.

4.1. Proton pump description and experiments

The proton pump (figure 2) is a particular ion pump that is able to change the pH level in a target solution through delivery of H^+ ions. This is a system with a nonlinear relation between the input and output response. The proton pump consists of two reservoirs: one is a source of charged ions H^+ , and another is a target reservoir that interfaces with a biological system.

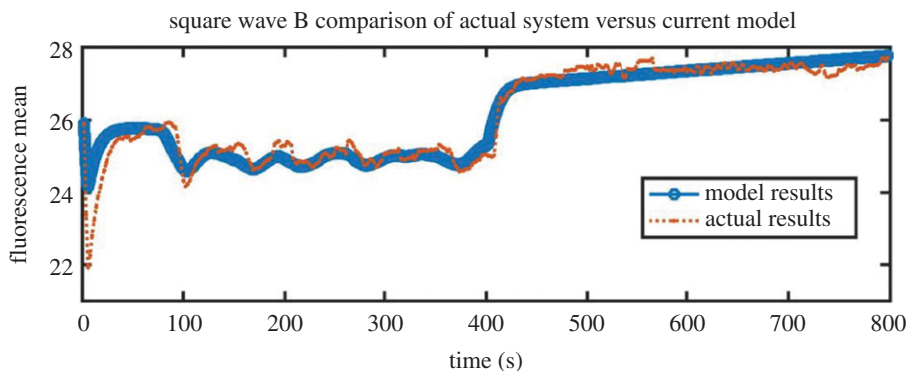


Figure 3. Simulation of the model compared with experimental data.

Applying voltage (V_{H^+}), as illustrated in figure 2, leads to redistribution of ions between (a) and (c). Changes in concentration of H^+ and, hence, pH of the target area are tracked with the aid of a fluorescent dye known as SNARF [32]. The mean pixel value of the fluorescent image of the target area can be mapped to output pH through a linear mapping derived through calibrations. In this case, the mapping is $\text{pH} = 0.0842\text{FMPV} + 4.9192$, where FMPV is the fluorescent mean pixel value. Ion concentration is mapped to pH by the relationship $\text{pH} = -\log_{10}[\text{H}^+]$. In order to map the ion concentration to the fluorescent image the two equations are combined to get $\text{FMPV} = -\log_{10}[\text{H}^+] - 4.9192/0.0842$.

The proton pump was housed within a microfluidic channel and the $[\text{H}^+]$ indicator SNARF-1 was loaded into the microfluidic channel with a syringe. Furthermore, the proton pump was connected to a Raspberry Pi controller board. This setup allowed for dynamic control over H^+ delivery in real-time. In this experimental set-up, the input (applied voltage) was determined by the feedback algorithm described in [19]. A baseline measurement of the fluorescence intensity (FI) in the microfluidic channel was recorded and used to set the starting value (FI = 25); the reference signal was programmed to be 5 fluorescence intensity units higher than this measured value (FI = 30). Over an experiment of 800 s, the fluorescent microscope collected images every 2 s. The voltage was moderated within the range of ± 1.7 V. This voltage range was selected to avoid excess electrolysis in the system. Here, we leverage only the input/output data generated in the experiment.

4.2. Proton pump modelling

Let x_{p_1} be the concentration of H^+ in the target area and x_{p_2} the H^+ concentration in reservoir (a) (figure 2). If no voltage is applied to the system, the ions are redistributed between the two volumes by diffusion. If control input voltage $\varphi(u)$ is applied, the ions move from one volume to another depending on the sign of $\varphi(u)$. The model of the proton pump may be written as

$$\text{and } \varphi(u) > 0 \begin{cases} \dot{x}_{p_1} = D(\hat{k}x_{p_2} - x_{p_1}) + \varphi(u) \frac{c_1 x_{p_2}}{d_1 + x_{p_2}} - g x_{p_1} \\ \dot{x}_{p_2} = D(x_{p_1} - \hat{k}x_{p_2}) - \varphi(u) \frac{c_1 x_{p_2}}{d_1 + x_{p_2}} \end{cases} \quad (4.1)$$

$$\text{and } \varphi(u) \leq 0 \begin{cases} \dot{x}_{p_1} = D(\hat{k}x_{p_2} - x_{p_1}) + \varphi(u) \frac{c_2 x_{p_1}}{d_2 + x_{p_1}} - g x_{p_1} \\ \dot{x}_{p_2} = D(x_{p_1} - \hat{k}x_{p_2}) - \varphi(u) \frac{c_2 x_{p_1}}{d_2 + x_{p_1}} \end{cases}$$

Table 1. Estimated parameters of the proton pump model.

parameters	values
D	0.1190
\hat{k}	0.1247
d_1	20.0000
d_2	6.6336
c_1	0.7868
c_2	0.0664
g	0.0039

where D is the diffusion coefficient, $c_{1,2}$ and $d_{1,2}$ are the parameters of the nonlinear functions, g is the leakage rate, \hat{k} is to keep an uneven equilibrium distribution without voltage due to the design of the proton pump and the saturated actuating function $\varphi(u)$ satisfies (2.4). The rate of voltage-driven ion exchange between the volumes is described by saturating nonlinear functions.

In order to estimate the parameters of the model, we fit the model to time series data mapping device input $\varphi(u)$ to output x_{p_1} using experimental data [18].

We used Grey-Box Estimation from the Matlab System Identification Toolbox for the model-data fitting procedure. An example of simulation of the model output and real measured data is shown in figure 3. The values of the estimated parameters are shown in table 1. The root mean square error (RMSE) is commonly used to measure the difference between a model and the data that the model is trying to capture. The formula for the RMSE is: $\sqrt{\sum_{i=1}^N (\hat{x}_i - x_i)^2 / N}$. The RMSE calculated for the simulation here is 0.3459 and might vary from one experiment to another.

4.3. Proton pump control

Our goal is to control proton concentration (x_{p_1}) in the targeted area (c) as depicted in figure 2. The proton pump model (4.1) can be represented in the form of system (2.1) as follows:

$$\text{and } \varphi(u) > 0 \begin{cases} \dot{x}_p = f(x_p) + G(x_p) \text{sat}(\varphi(u)) \\ y_p = x_{p_1} \end{cases} \quad (4.2)$$

$$\text{and } \varphi(u) \leq 0 \begin{cases} \dot{x}_p = f'(x_p) + G'(x_p) \text{sat}(\varphi(u)) \\ y_p = x_{p_1} \end{cases}$$

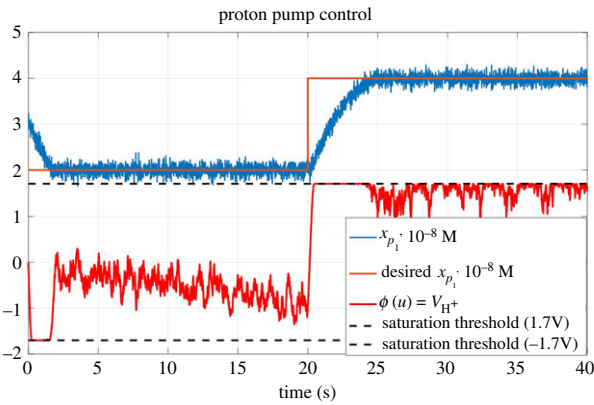


Figure 4. Setpoint regulation for the proton pump model with white noise using the proposed control scheme.

where

$$\text{and } \varphi(u) > 0 \left\{ \begin{array}{l} f(x_p) = \begin{bmatrix} D(\hat{k}x_{p_2} - x_{p_1}) - gx_{p_1} \\ D(x_{p_1} - \hat{k}x_{p_2}) \end{bmatrix} \\ G(x_p) = \begin{bmatrix} \frac{c_1 x_{p_2}}{d_1 + x_{p_2}} \\ -\frac{c_1 x_{p_2}}{d_1 + x_{p_2}} \end{bmatrix} \end{array} \right. \\ \text{and } \varphi(u) \leq 0 \left\{ \begin{array}{l} f'(x_p) = \begin{bmatrix} D(\hat{k}x_{p_2} - x_{p_1}) - gx_{p_1} \\ D(x_{p_1} - \hat{k}x_{p_2}) \end{bmatrix} \\ G'(x_p) = \begin{bmatrix} \frac{c_2 x_{p_1}}{d_2 + x_{p_1}} \\ -\frac{c_2 x_{p_1}}{d_2 + x_{p_1}} \end{bmatrix} \end{array} \right. \quad (4.3)$$

We apply the control scheme developed in theorem 3.6 to regulate x_{p_1} . We note that bioelectronic devices in general are ISS, the corresponding matrix $Q^T Q$ is non-singular, and, furthermore, \dot{x}_{p_1} and \dot{x}_{p_2} are bounded. This implies the existence of a gain ρ' for convergence.

We design v according to (3.23), where $C = [1 \ 0]$ or $y = x_{p_1}$. The only information we need from the proton pump model is the sign value of $CG(x_p)$ and $CG'(x_p)$, which are both positive given x_{p_1} and x_{p_2} represent proton concentrations and are positive. Based on the common Lyapunov function theorem in switching systems [33], as long as there exists a gain ρ' such that the inequality (3.22) holds for both systems in (4.2), then convergence is guaranteed according to theorem 3.6. The desired manifold is

$$s' = k(x_{p_1} - x_{p_{1,d}}) + (\dot{x}_{p_1} - \dot{x}_{p_{1,d}}) \quad (4.4)$$

with $k = 1$. We set $\rho' = 2$ and $\varphi(u) = 1.7\sin(u)$, where 1.7 is the pump actuation threshold voltage.

Choosing $\varphi(u) = 1.7\sin(u)$ over a monotonic function (e.g. logistic function) has the advantage of avoiding convergence of $\nabla_u \varphi(u)$ to zero (i.e. avoiding singularity of $Q^T Q$) as $u \rightarrow \infty$. Furthermore, the set of $u = \{u \in \mathbb{R} \mid \nabla_u \varphi(u) = 1.7\cos(u) = 0\}$ has measure zero and does not affect convergence results [34].

Two numerical simulations are conducted in MATLAB Simulink to verify the performance of our proposed control scheme on the proton pump, one for setpoint regulation (figure 4) and another one for sinusoidal trajectory tracking (figure 5).

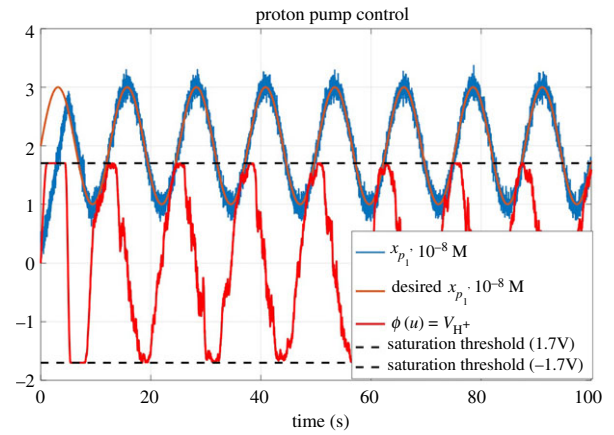


Figure 5. Trajectory tracking for proton pump model with white noise using the proposed control scheme.

5. Wound healing process modelling and control

5.1. Ions and wound healing

There are several stages of wound healing, of which the most important are inflammation and reparation. During inflammation the immune system cleans the wound of debris and infection. The recovery stage may be represented as proliferation and reparation; during this stage new tissue replaces damaged tissue. In some cases, the transition from inflammation to recovery does not occur and the wound becomes chronic [28].

Controlled supply of ions may be promising in wound healing care. For example, sodium ions are important for immune reaction against pathogens; however, excess sodium prevents tissue reparation [35]. Potassium ions may exert an anti-inflammatory effect on macrophages [36] and pH, defined by the concentration of H^+ ions, is important both for inflammation and for tissue reparation [29,37]. As summarized in [29], during inflammation, wound pH gradually decreases to approx. 5.5 and then rises to 7.5–8 at the end of granulation tissue formation. After that, in acute wounds pH returns to 6–6.5 during re-epithelialization, and in chronic wounds pH stays at approx. 7.5. The growth of pathogen microorganisms is decreased at low pH [38]. Furthermore, the activity of many proteases needed for extracellular matrix reorganization is pH-sensitive [39]. If the activity of proteases does not diminish at the appropriate stage of reparation, chronic inflammation can ensue [29].

5.2. A mathematical model of wound healing

In order to test applicability of the controller to wound healing, we propose a phenomenological model of wound healing. The wound is represented as a bistable system: one stable point corresponds to healthy tissue and another stable point represents the chronic situation. At the initial time of injury, the system begins to move towards the healthy stable equilibrium point. However, in some cases, the system may be attracted to the chronic state, which corresponds to the wound not healing. The model of wound healing consists of two equations:

$$\text{and } \left. \begin{array}{l} \dot{x}_1 = -(x_1 - x_2)(x_1 - x_2 - \delta)(x_1 - 1) \\ \dot{x}_2 = -\gamma x_2, \quad \gamma > 0, \end{array} \right\} \quad (5.1)$$

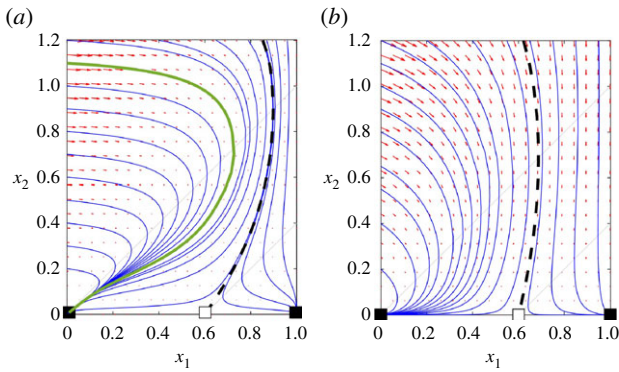


Figure 6. Phase portrait of wound healing model, $\delta = 0.6$. (a) $\gamma = 0.1$, (b) $\gamma = 0.7$. Dashed black lines—separatrix dividing basins of attraction of healthy $(0, 0)$ and chronic $(1, 0)$ stable states. Green line—one of trajectories corresponding to normal wound healing.

where $0 \leq x_1 \leq 1$ is a measurement of inflammation with $x_1 = 0$ indicating a healthy state and $x_1 > 0$ corresponding to inflammation. Let $x_2 \geq 0$ be a wound media variable that defines the state of the wound, and γ is the degradation factor for x_2 . For example, wound pH is known to decrease during inflammation [29], i.e. concentration of H^+ ions increases during inflammation.

System (5.1) has three equilibrium points $(0, 0)$, $(\delta, 0)$, $(1, 0)$, representing healed, intermediate and chronic situations, respectively. Applying the first method of Lyapunov shows equilibrium points $(0, 0)$, $(1, 0)$ are stable and $(\delta, 0)$ is an unstable equilibrium point. Based on initial conditions, natural wound healing can converge to the healed or chronic situation (figure 6a).

A naive approach to accelerating wound healing might be to increase the degradation rate γ . However, note that increasing the degradation rate γ changes the shape of the separatrix such that wound healing may be accelerated but the basin of attraction for healthy wound healing is decreased (figure 6b). Wound healing trajectories are fastest near the separatrix but in a noisy system an amplified system response poses the added risk of being pushed to a chronic state. In the next section, we present a hybrid controller that accelerates wound healing, while minimizing the risk of chronic inflammation.

5.3. Wound healing control

Our control goals are twofold. First, we would like to increase the basin of attraction for the equilibrium point $(0, 0)$ representing healthy tissue. In this way, we can avoid a chronic situation independent of the initial condition. Second, we would like to accelerate wound healing. We assume that we can manipulate x_2 but not x_1 . However, we assume that sensing is available for both variables.

To control wound healing via a bioelectronic device, we use the control architecture shown in figure 7. A model of wound healing directed by a bioelectronic ion pump can be generally written as

$$\left. \begin{aligned} \dot{x}_1 &= -(x_1 - x_2)(x_1 - x_2 - \delta)(x_1 - 1) \\ \dot{x}_2 &= -\gamma x_2 + w_1(x_1, x_2) - w_2(x_1, x_2) \end{aligned} \right\} \quad (5.2)$$

and $y = x_1$,

where $w_1(x_1, x_2) = x_{p_1}$ and $w_2(x_1, x_2) = x'_{p_1}$ are the concentration of distinct ions delivered by a bioelectronic device. We let w_1 represent additional proton injection and w_2

represent a second charged molecule that neutralizes H^+ . In this section, we derive the feedback control laws $w_1(x_1, x_2)$ and $w_2(x_1, x_2)$ that do not violate any physical or biological constraints, while accelerating wound healing. The bioelectronic device is then tasked with tracking these desired concentrations. Our main goal here is to design x_{p_1} to avoid chronic equilibrium point for almost any initial value, and then design x'_{p_1} to accelerate healing time when we are in the basin of attraction of the equilibrium point representing healthy tissue.

We propose the following control design for (5.2):

$$\begin{bmatrix} x_{p_1} \\ x'_{p_1} \end{bmatrix} = \begin{cases} \begin{bmatrix} k_1 x_1 \\ 0 \end{bmatrix} \gamma(1 - \delta) < k_1 < \gamma, & \text{if } x_1 + x_2 \geq \delta \\ \begin{bmatrix} 0 \\ k_2 x_2 \end{bmatrix} k_2 > 0, k_2 > 2\delta - \gamma, & \text{if } x_1 + x_2 < \delta \end{cases} \quad (5.3)$$

which we will show guarantees that the closed-loop system trajectory (x_1, x_2) converges to $(0, 0)$ regardless of initial value and is accelerated in the region $x_1 + x_2 < \delta$. We also note that positivity of the system is conserved. That is, $x_1 \geq 0$ and $x_2 \geq 0$. Two bioelectronic ion pump controllers can be designed separately based on theorem 3.6 and control law (3.23) to make x_{p_1} (H^+ concentration) follow x_{p_1} in the first ion pump (proton pump) and x'_{p_1} (molecule/ion concentration that neutralizes H^+) follow x'_{p_1} in the second ion pump.

Our first goal is to increase the basin of attraction for healthy tissue (chronic avoidance). The following controller ensures system (5.2) converges to $(0, 0)$ independent of the initial value:

$$\left. \begin{aligned} w_1(x_1, x_2) &= k_1 x_1, & \gamma(1 - \delta) < k_1 < \gamma \\ \text{and } w_2(x_1, x_2) &= 0. \end{aligned} \right\} \quad (5.4)$$

System (5.2) and (5.4) preserves the stable equilibrium point $(0, 0)$ representing healthy tissue, while shifting the unstable point to $(1, (k_1/\gamma))$ and the stable point representing chronic inflammation to $((\delta\gamma/\gamma - k_1) > 1, (\delta k_1/\gamma - k_1))$. Figure 8 depicts the closed-loop phase plane of the healing process with $\gamma = 1$, $k_1 = 0.6$ and $\delta = 0.6$, where for $0 < x_1, x_2 < 1$ all trajectories go to $(0, 0)$.

The next goal is to accelerate the healing process (while maintaining convergence to $(0, 0)$) by increasing the rate of decay for x_2 .

Setting

$$\left. \begin{aligned} w_1(x_1, x_2) &= 0 \\ \text{and } w_2(x_1, x_2) &= k_2 x_2, & k_2 > 0, k_2 > 2\delta - \gamma \end{aligned} \right\} \quad (5.5)$$

preserves $(0, 0)$ as a stable equilibrium point. To find the basin of attraction for $(0, 0)$ under (5.5), we define the Lyapunov function candidate (given $x_{1,2} \geq 0$)

$$V(x_1, x_2) = x_1 + x_2. \quad (5.6)$$

The derivative of $V(x_1, x_2)$ along the system described by (5.2) and (5.5) is

$$\begin{aligned} \dot{V}(x_1, x_2) &= \dot{x}_1 + \dot{x}_2 \\ &= -(x_1 - x_2)(x_1 - x_2 - \delta)(x_1 - 1) - \gamma x_2 - k_2 x_2. \end{aligned} \quad (5.7)$$

We show the set $\Omega_B = \{x_1, x_2 \in \mathbb{R}^+ \cup \{0\} \mid x_1 + x_2 < \delta\} = \Omega_{B_1} \cup \Omega_{B_2} = \{x_1, x_2 \in \mathbb{R}^+ \cup \{0\} \mid x_1 + x_2 < \delta \cap x_1 - x_2 \geq 0\}$

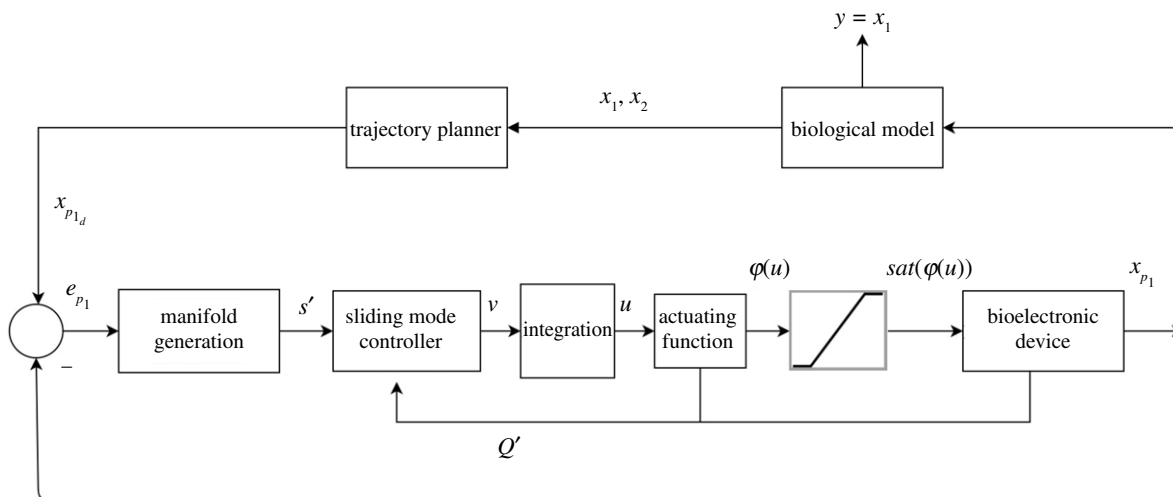


Figure 7. Closed loop control architecture of a biological process actuated by a bioelectronic device with input saturation.

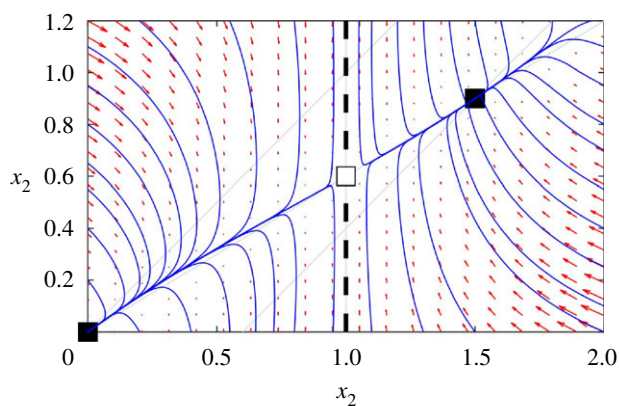


Figure 8. Phase plane of states x_1 and x_2 for $\delta = 0.6$, $\gamma = 1$ and $k_1 = 0.6$ for system (5.4) with a single ion pump.

$\cup\{x_1, x_2 \in \mathbb{R}^+ \cup \{0\} \mid x_1 + x_2 < \delta \cap x_1 - x_2 < 0\}$ is a basin of attraction to $(0, 0)$ for (5.2) and (5.5). As $0 \leq x_1 \leq 1$ and $x_2 \geq 0$, in Ω_{B_1}

$$\left. \begin{aligned} x_1 - x_2 &\geq 0 \\ x_1 - 1 &\leq 0 \\ \text{and } x_1 - x_2 - \delta &\leq x_1 + x_2 - \delta < 0 \end{aligned} \right\} \quad (5.8)$$

which means $\dot{V}(x_1, x_2) < 0$ for x_1 and x_2 in Ω_{B_1} except $(0, 0)$. In Ω_{B_2}

$$\left. \begin{aligned} x_1 - x_2 &< 0 \\ x_1 - 1 &\leq 0 \\ \text{and } x_1 - x_2 - \delta &\leq x_1 + x_2 - \delta < 0 \end{aligned} \right\} \quad (5.9)$$

and $\dot{V}(x_1, x_2)$ can be upper bounded as below

$$\dot{V}(x_1, x_2) < -2\delta(x_1 - x_2) - (\gamma + k_2)x_2, \quad (5.10)$$

because $x_1 > 0$

$$\dot{V}(x_1, x_2) < 2\delta x_2 - (\gamma + k_2)x_2, \quad (5.11)$$

and as $k_2 > 2\delta - \gamma$ in (5.5) and $x_2 \geq 0$, $\dot{V} < 0$ in Ω_{B_2} except at $(0, 0)$.

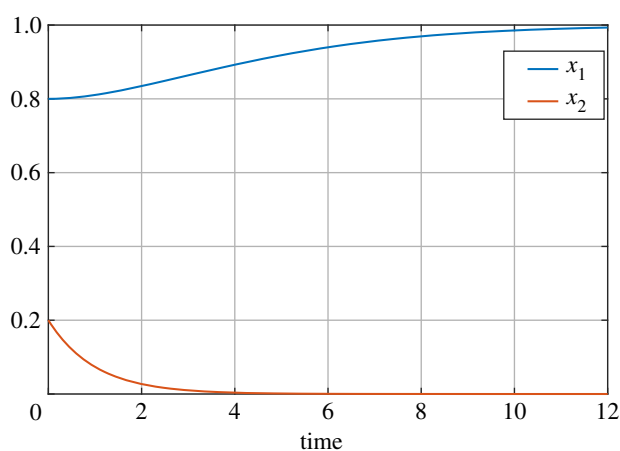


Figure 9. Natural wound healing trajectories based on system (5.1) for initial value close to the chronic situation and for $\delta = 0.6$, $\gamma = 1$.

6. Simulations

In this section, a set of simulations are conducted on the phenomenological wound healing model (5.1), both open-loop and closed-loop, to verify the effectiveness of our proposed method including chronic situation avoidance and healing process acceleration.

6.1. Natural healing process

Figure 9 shows x_1 and x_2 trajectories for an initial value close to the chronic situation based on model (5.1) and with no control input. It can be observed that wound converges to chronic point ($x_1 = 1$) and x_2 goes to zero. This stable equilibrium point is undesirable and a closed-loop regulation is needed to avoid it.

6.2. Closed-loop healing process with a single ion pump

In this simulation, one ion pump (with existence of white noise) is used to regulate proton injection to avoid the chronic situation based on (5.4). Figure 10 indicates the ion pump control voltage signal, the desired proton concentration and the measured proton concentration, which converges to desired one. Figure 11 depicts system trajectories of the wound, which converge to the healed point $(0, 0)$ as desired.

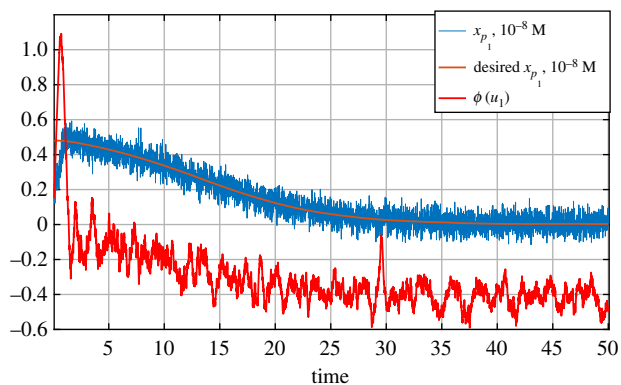


Figure 10. Closed-loop ion concentration and control signal for initial value close to the chronic situation and for $\delta = 0.6$, $\gamma = 1$, $k_1 = 0.6$ in system (5.4) with a single ion pump.

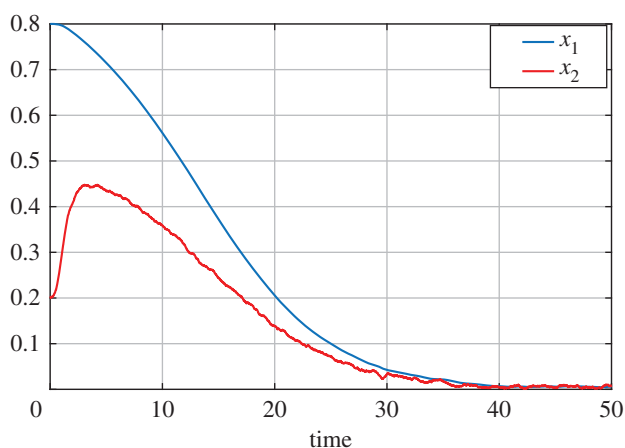


Figure 11. Closed-loop wound healing trajectories for system (5.4) with a single ion pump with initial value close to the chronic situation and for $\delta = 0.6$, $\gamma = 1$ and $k_1 = 0.6$.

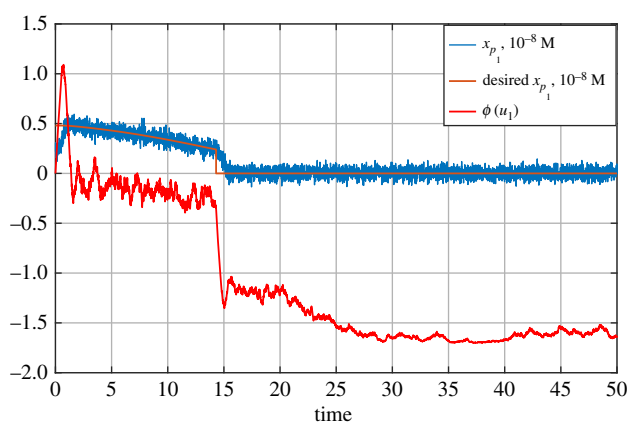


Figure 12. Closed-loop ion concentration and control signal for the first ion pump in system (5.3) with initial value close to the chronic situation and for $\delta = 0.6$, $\gamma = 1$, $k_1 = 0.6$.

6.3. Closed-loop healing process with two ion pumps

Two ion pumps are controlled here based on system (5.3). Figure 12 shows the control signal for the first ion pump regulating proton injection. Figure 13 shows the second ion pump control signal regulating x'_{p1} delivery. Figure 14 shows accelerated convergence to $(0, 0)$ when compared with figure 11 for the single ion pump system (5.4). Accelerated wound healing is achieved with the second ion pump which increases x_2 decay rate.

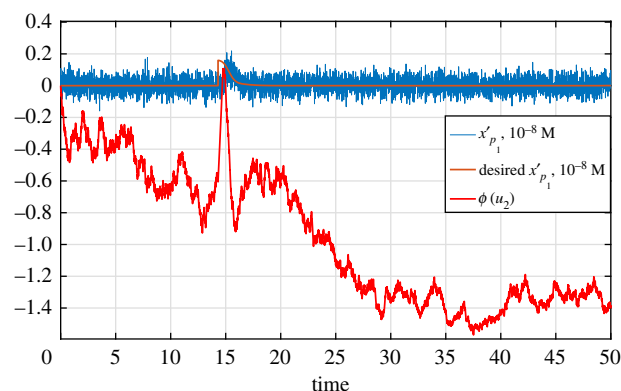


Figure 13. Closed-loop ion concentration and control signal for the second ion pump in system (5.3) with initial value close to the chronic situation and for $\delta = 0.6$, $\gamma = 1$, $k_2 = 0.6$.

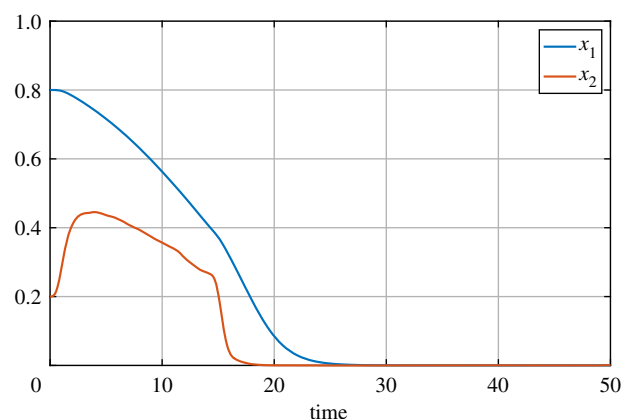


Figure 14. Closed-loop accelerated wound healing trajectories for initial value close to the chronic situation and for $\delta = 0.6$, $\gamma = 1$ and $k_{1,2} = 0.6$ for system (5.3).

7. Conclusion

In summary, we propose that an effective approach to controlling complex biological processes interfaced with a bioelectronic device is through a modular control architecture. The modular feedback control architecture allows one to design the controller for the bioelectronic device independent of the biological process in the loop. That is, our controller design does not have any dependence on the wound healing model. The wound healing model is instead used to inform the desired wound environment to be achieved by the bioelectronic device. We note that the time scale of the dynamical response of the bioelectronic device to changes in voltages is orders of magnitude faster than that of biological processes in wound healing. Thus, we do not need to be concerned with the required changes in pH for accelerated wound healing happening at a time scale faster than convergence of the controller. The bioelectronic device is controlled through a novel saturated-based sliding mode control method and its respective reference signal is designed based on a desired biological response. We applied this method to a bistable phenomenological model of wound healing. In this work, we used Lyapunov analysis and phase plane trajectory design to generate the reference signal for the bioelectronic device in order to avoid chronic wounds and achieve accelerated wound closure. We note that many biological systems exhibit multistable behaviour [40] and, thus, our results can generalize to a broader range of applications. Finally, in the future, we will explore

data-driven methods to generate reference trajectories in real-time for optimal wound closure.

Data accessibility. Our paper uses data generated in another publication to fit parameters in a model. The data are contained within the following papers: <https://onlinelibrary.wiley.com/doi/full/10.1002/aisy.202000140> and <https://ieeexplore.ieee.org/abstract/document/9163327>.

Authors' contributions. B.H.J., K.Z. and M.G. contributed to the design and implementation of the research, conceived the presentation of the work, and led the writing of the manuscript. B.H.J. developed the control architecture and sliding mode control design. B.H.J. and M.G. developed the stability proof. G.M. led the development of the model of the bioelectronic device in collaboration with B.H.J. and M.Ja. K.Z. led the development of the wound healing model in collaboration with B.H.J. and M.Ja. B.H.J. led the work on integrating the models and simulating the systems with the sliding mode controller. M.Ji., J.S. and M.Ja. ran experiments on the bioelectronic device, which produced data used for parameter fitting. M.R. designed the bioelectronic devices and secured funding. All authors discussed the results and contributed to the final manuscript.

Competing interests. We declare we have no competing interests.

Funding. Research was sponsored by the Office of Naval Research and the DARPA Biotechnologies Office (DARPA/BTO) and was accomplished under Cooperative agreement no. DC20AC00003.

Acknowledgements. The authors thank all active collaborators who have engaged us in conversations on the topic of wound healing, including Dr Rivkah Isseroff, Dr Min Zhao, and their laboratory affiliates at UC Davis.

Disclaimer. The views and conclusions contained in this document are those of the authors and should not be interpreted as representing the official policies, either expressed or implied, of the Office of Naval Research and the DARPA Biotechnologies Office (DARPA/BTO) or the US Government. The US Government is authorized to reproduce and distribute reprints for Government purposes notwithstanding any copyright notation herein.

Appendix A

Ion pumps are bioelectronic devices that interface with biological systems by controlling the concentration of ions in solution. Ion pumps can be tuned for control of a specific ionic species such as protons to change pH. The means of operation for an ion pump is the application of an electric field to induce electrophoretic movement of ions into a target solution. In this case, a Raspberry Pi controller running a control algorithm is used to drive the voltage on the electrodes of an ion pump array built within a microfluidic channel (figures 2 and 15). The device's microfluidic channel is loaded with a pH-responsive fluorescent dye solution (SNARF-1), images are captured with a fluorescence microscope (figure 16). The mean pixel value of the target area from the new image is computed and mapped to ion concentration in the target area. This value is fed back to the ion pump controller and is used to drive the ion concentration in solution to a pre-prescribed step function using a closed-loop control algorithm. The ion pump array operates by applying a voltage between palladium-coated array electrodes located beneath a polyelectrolyte ion bridge and Ag/AgCl electrodes in the target microfluidic channel. The palladium electrodes selectively absorb and release H^+ due to a material property of palladium and this confers selectivity and efficiency to the system. The ion bridge that covers the palladium electrode array spans the gap between a reservoir channel and a target microfluidic channel and acts as a H^+ source for the system. When a positive voltage is applied

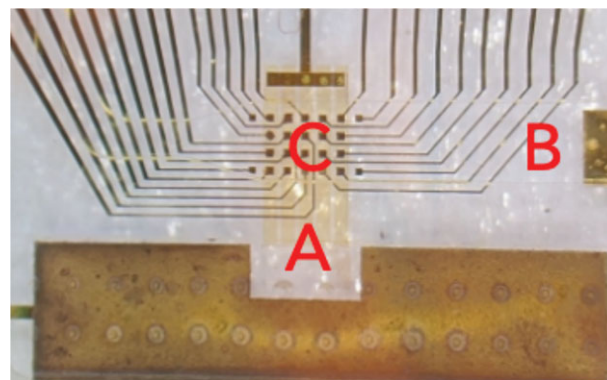


Figure 15. Optical image of actual device. Panel (c) Represents the area where microscopic readings are taken. This is a 5×5 array where voltages can be applied to change pH in the target area.

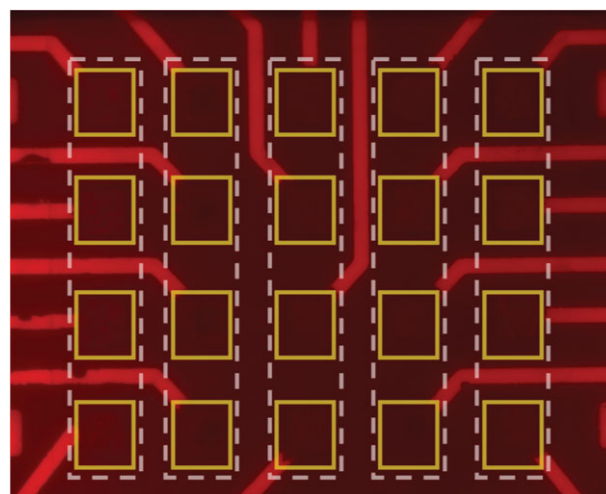


Figure 16. Optical image from the microscope. The dashed lines are the columns where microelectrodes are located and can be actuated.

between the palladium electrode array and the Ag/AgCl counter electrodes, H^+ are released from the ion bridge into the target solution. When a negative voltage is applied, the protons are pulled back into the ion bridge and are absorbed by palladium, forming palladium hydride. The ion pumps were connected to the Raspberry Pi controller board with a custom adapter and $50 \mu M$ of the $[H^+]$ indicator SNARF-1 dispensed in 0.1M Tris buffer was loaded into the microfluidic channel with a syringe. SNARF-1 indicator has a fluorescence intensity magnitude that is sensitive to pH. The ion pump was fitted onto a BZ-X710 fluorescence microscope (objectives: excitation 560/40 nm, emission 630/75 nm) stage with a custom acrylic adapter. A baseline measurement of the fluorescence intensity (FI) in the microfluidic channel was recorded and used to set the starting value in a step function ($FI = 25$), the step was programmed to be 5 fluorescence intensity units higher than this measured value ($FI = 30$). Over an experiment of 800 s, the fluorescent microscope collected images every 2 s and the mean pixel fluorescence intensity value from the target area was computed and fed back to the ion pump control algorithm. The control algorithm responded to error in the expected and real fluorescent values of the device by modulating the voltage within the range of ± 1.7 V. This voltage range was selected to avoid excess electrolysis in the system.

- Löffler S, Melican K, Nilsson K, Richter-Dahlfors A. 2017 Organic bioelectronics in medicine. *J. Intern. Med.* **282**, 24–36. (doi:10.1111/joim.2017.282.issue-1)
- Wu H, Gao W, Yin Z. 2017 Materials, devices and systems of soft bioelectronics for precision therapy. *Adv. Healthcare Mater.* **6**, 1700017. (doi:10.1002/adhm.v6.10)
- Birmingham K *et al.* 2014 Bioelectronic medicines: a research roadmap. *Nat. Rev. Drug Discov.* **13**, 399–400. (doi:10.1038/nrd4351)
- Selberg J, Jafari M, Bradley C, Gomez M, Rolandi M. 2020 Expanding biological control to bioelectronics with machine learning. *APL Mater.* **8**, 120904. (doi:10.1063/5.0027226)
- Jia M, Rolandi M. 2020 Soft and ion-conducting materials in bioelectronics: from conducting polymers to hydrogels. *Adv. Healthc. Mater.* **9**, 1901372. (doi:10.1002/adhm.v9.5)
- Mostafalu P. 2018 Smart bandage for monitoring and treatment of chronic wounds. *Small* **14**, e1703509. (doi:10.1002/smll.v14.33)
- Farooqui MF, Shamim A. 2016 Low cost inkjet printed smart bandage for wireless monitoring of chronic wounds. *Sci. Rep.* **6**, 28949. (doi:10.1038/srep28949)
- McLister A, McHugh J, Cundell J, Davis J. 2016 New developments in smart bandage technologies for wound diagnostics. *Adv. Mater.* **28**, 5732–5737. (doi:10.1002/adma.v28.27)
- Sharp D, Gladstone P, Smith RB, Forsythe S, Davis J. 2010 Approaching intelligent infection diagnostics: carbon fibre sensor for electrochemical pyocyanin detection. *Bioelectrochemistry* **77**, 114–119. (doi:10.1016/j.bioelechem.2009.07.008)
- Williamson A *et al.* 2015 Controlling epileptiform activity with organic electronic ion pumps. *Adv. Mater.* **27**, 3138–3144. (doi:10.1002/adma.201500482)
- Proctor CM, Chan CY, Porcarelli L, Udabe E, Sanchez-Sanchez A, Del Agua I, Mecerreyes D, Malliaras GG. 2019 Ionic hydrogel for accelerated dopamine delivery via retrodialysis. *Chem. Mater.* **31**, 7080–7084. (doi:10.1021/acs.chemmater.9b02135)
- Jonsson A, Song Z, Nilsson D, Meyerson BA, Simon DT, Linderöth B, Berggren M. 2015 Therapy using implanted organic bioelectronics. *Sci. Adv.* **1**, e1500039. (doi:10.1126/sciadv.1500039)
- El-Khatib FH, Russell SJ, Nathan DM, Sutherland RG, Damiano ER. 2010 A bihormonal closed-loop artificial pancreas for type 1 diabetes. *Sci. Transl. Med.* **2**, 27ra27. (doi:10.1126/scitranslmed.3000619)
- Quiroz G. 2019 The evolution of control algorithms in artificial pancreas: a historical perspective. *Annu. Rev. Control* **48**, 222–232. (doi:10.1016/j.arcontrol.2019.07.004)
- Santaniello S, Fiengo G, Glielmo L, Grill WM. 2010 Closed-loop control of deep brain stimulation: a simulation study. *IEEE Trans. Neural Syst. Rehabil. Eng.* **19**, 15–24. (doi:10.1109/TNSRE.7333)
- Malliaras G, Abidian MR. 2015 Organic bioelectronic materials and devices. *Adv. Mater. (Deerfield Beach, Fla)* **27**, 7492. (doi:10.1002/adma.v27.46)
- Noy A. 2015 Mimicking biology with nanomaterials: carbon nanotube porins in lipid membranes. *Biophys. J.* **108**, 443a. (doi:10.1016/j.bpj.2014.11.2418)
- Jafari M, Marquez G, Selberg J, Jia M, Dechiraju H, Pansodtee P, Teodorescu M, Rolandi M, Gomez M. 2020 Feedback control of bioelectronic devices using machine learning. *IEEE Control Syst. Lett.* **5**, 1133–1138. (doi:10.1109/LCSYS.7782633)
- Selberg J *et al.* 2020 Machine learning-driven bioelectronics for closed-loop control of cells. *Adv. Intell. Syst.* **2**, 2000140. (doi:10.1002/aisy.v2.12)
- Farrell J, Polycarpou M, Sharma M. 2004 On-line approximation based control of uncertain nonlinear systems with magnitude, rate and bandwidth constraints on the states and actuators. In *Proc. of the 2004 American Control Conf.*, vol. 3, pp. 2557–2562. New York, NY: IEEE.
- Wen C, Zhou J, Liu Z, Su H. 2011 Robust adaptive control of uncertain nonlinear systems in the presence of input saturation and external disturbance. *IEEE Trans. Autom. Control* **56**, 1672–1678. (doi:10.1109/TAC.2011.2122730)
- Chen M, Ge SS, Ren B. 2011 Adaptive tracking control of uncertain MIMO nonlinear systems with input constraints. *Automatica* **47**, 452–465. (doi:10.1016/j.automatica.2011.01.025)
- Zhou S, Chen M, Ong CJ, Chen PC. 2016 Adaptive neural network control of uncertain MIMO nonlinear systems with input saturation. *Neural Comput. Appl.* **27**, 1317–1325. (doi:10.1007/s00521-015-1935-7)
- Chen M, Ge SS, How BVE. 2010 Robust adaptive neural network control for a class of uncertain MIMO nonlinear systems with input nonlinearities. *IEEE Trans. Neural Netw.* **21**, 796–812. (doi:10.1109/TNN.2010.2042611)
- Chen Z, Li Z, Chen CP. 2016 Adaptive neural control of uncertain MIMO nonlinear systems with state and input constraints. *IEEE Trans. Neural Netw. Learn. Syst.* **28**, 1318–1330. (doi:10.1109/TNNLS.2016.2538779)
- Canedo-Dorantes L, Canedo-Ayala M. 2019 Skin acute wound healing: a comprehensive review. *Int. J. Inflamm.* **2019**, 3706315. (doi:10.1155/2019/3706315)
- Wokalek H, Ruh H. 1991 Time course of wound healing. *J. Biomater. Appl.* **5**, 337–362. (doi:10.1177/088532829100500405)
- Krzyszczak P, Schloss R, Palmer A, Berthiaume F. 2018 The role of macrophages in acute and chronic wound healing and interventions to promote pro-wound healing phenotypes. *Front. Physiol.* **9**, 419. (doi:10.3389/fphys.2018.00419)
- Schneider LA, Korber A, Grabbe S, Dissemond J. 2007 Influence of pH on wound-healing: a new perspective for wound-therapy? *Arch. Dermatol. Res.* **298**, 413–420. (doi:10.1007/s00403-006-0713-x)
- Sharpe J, Harris K, Jubin K, Bainbridge N, Jordan N. 2009 The effect of pH in modulating skin cell behaviour. *Br. J. Dermatol.* **161**, 671–673. (doi:10.1111/bjd.2009.161.issue-3)
- Khalil HK, Grizzle JW. 2002 *Nonlinear systems*, vol. 3. Upper Saddle River, NJ: Prentice Hall.
- Whitaker JE, Haugland RP, Prendergast FG. 1991 Spectral and photophysical studies of benzo[c]xanthene dyes: dual emission pH sensors. *Anal. Biochem.* **194**, 330–344. (doi:10.1016/0003-2697(91)90237-N)
- Liberzon D. 2003 *Switching in systems and control*. New York, NY: Springer Science & Business Media.
- Royden HL, Fitzpatrick P. 1988 *Real analysis*, vol. 32. New York, NY: Macmillan.
- Wilck N, Balogh A, Marko L, Bartolomeaus H, Muller DN. 2019 The role of sodium in modulating immune cell function. *Nat. Rev. Nephrol.* **15**, 546–558. (doi:10.1038/s41581-019-0167-y)
- Erndt-Marino J, Yeisley DJ, Chen H, Levin M, Kaplan DL, Hahn MS. 2020 Interferon-gamma stimulated murine macrophages *in vitro*: impact of ionic composition and osmolarity and therapeutic implications. *Bioelectricity* **2**, 48–58. (doi:10.1089/bioe.2019.0032)
- Schremel S, Szeimies RM, Karrer S, Heinlin J, Landthaler M, Babilas P. 2010 The impact of the pH value on skin integrity and cutaneous wound healing. *Eur. Acad. Dermatol. Venereol.* **24**, 373–378. (doi:10.1111/jdv.2010.24.issue-4)
- Thomas LV, Wimpenny JW, Davis JG. 1993 Effect of three preservatives on the growth of *Bacillus cereus*, *Vero* cytotoxicigenic *Escherichia coli* and *Staphylococcus aureus*, on plates with gradients of pH and sodium chloride concentration. *Int. J. Food Microbiol.* **17**, 289–301. (doi:10.1016/0168-1605(93)90199-Q)
- Greener B, Hughes AA, Bannister NP, Douglass J. 2005 Proteases and pH in chronic wounds. *J. Wound Care* **14**, 59–61. (doi:10.12968/jowc.2005.14.2.26739)
- Angeli D, Ferrell JJE, Sontag ED. 2004 Detection of multistability, bifurcations, and hysteresis in a large class of biological positive-feedback systems. *Proc. Natl Acad. Sci. USA* **101**, 1822–1827. (doi:10.1073/pnas.0308265100)